PHOTONICS Research

Ultrafast photocarrier and coherent phonon dynamics in type-II Dirac semimetal $PtTe_2$ thin films probed by optical spectroscopy

Peng Suo,[1] Shengnan Yan,[2] Ruihua Pu,[3] Wenjie Zhang,[1] Di Li,[1] Jiaming Chen,[1] Jibo Fu,[1] Xian Lin,[1] Feng Miao,[2] Shi-Jun Liang,[2] Weimin Liu,[3,4] and Guohong Ma[1,*]

[1]Department of Physics, Shanghai University, Shanghai 200444, China
[2]National Laboratory of Solid State Microstructures, School of Physics, Collaborative Innovation Center of Advanced Microstructures, Nanjing University, Nanjing 210093, China
[3]School of Physical Science and Technology, ShanghaiTech University, Shanghai 201210, China
[4]e-mail: liuwm@shanghaitech.edu.cn
*Corresponding authors: ghma@staff.shu.edu.cn

Received 3 September 2021; revised 3 December 2021; accepted 6 January 2022; posted 7 January 2022 (Doc. ID 442114); published 17 February 2022

We report the ultrafast photocarrier dynamics and coherent phonon excitation in type-II Dirac semimetal platinum ditelluride ($PtTe_2$) thin films via femtosecond (fs) pump-probe spectroscopy at room temperature. Quantitative analysis revealed that the incoherent electronic relaxation consists of two components: a subpicosecond fast relaxation process and a slow component with a time constant of hundreds of picoseconds (ps). Furthermore, the launch of a coherent acoustic phonon (CAP) in the 20 nm film but absence in the 6.8 nm film uncovers the dominant role of temperature gradient in producing a strain wave. The sound velocity and Young's modulus in the thick $PtTe_2$ are determined to be 1.736 km/s and 29.5 GPa, respectively. In addition, the coherent optical phonon (COP) with a frequency of 4.7 THz corresponding to Te atoms out-of-plane A_{1g} vibration has been well resolved in all films, which is ascribed to displacive excitation of coherent phonon (DECP). The observation of a strong probe-wavelength dependent COP amplitude reveals the resonant feature of the optical excitation-induced atomic displacement in $PtTe_2$. Our findings provide deep insight into the excitation and dynamics of CAP and COP as well as the photocarriers' recovery pathway and lifetimes in $PtTe_2$. Our study also demonstrates that the COP spectroscopy is a powerful tool to reveal the modulation of frequency-dependent optical constants induced by atomic vibrations, which may find applications in the fields of optoelectronics and ultrafast photonics.

https://doi.org/10.1364/PRJ.442114

1. INTRODUCTION

The experimental discovery of topological 3D Dirac semimetals (DSMs) provides unprecedented opportunities for investigating intriguing topological phase transition and various exotic quantum states in condensed matter [1–5]. According to the relative magnitude of potential and kinetic energy components of the Hamiltonian of Dirac fermions, the 3D DSMs are classified to type-I and type-II DSMs [6,7]. The noble transition-metal dichalcogenide (TMD) $PtTe_2$ has been identified as a typical type-II DSM with anisotropic and heavily tilted Dirac cones and stands out from other DSM materials due to the topological nontrivial band structure [7,8], ultrahigh electrical conductivity [9,10], and robustness of the remaining semimetal even down to just two triatomic layers [11,12]. Lately, doped $Pt_{1-x}Ir_xTe_2$ has realized the Fermi level tunability and superconductivity, which opens up a new route for the investigation of Dirac physics and topological superconductivity [13,14]. More recently, $PtTe_2$-based broadband photodetectors and image sensors have been fabricated, demonstrating tremendous application value in various photoelectric devices [15–17]. Therefore, the study of $PtTe_2$ cannot only reveal novel condensed-matter physics but also facilitate the versatile development in device physics.

In our previous work, the negative terahertz photoconductivity in $PtTe_2$ was observed and studied using optical pump-terahertz probe spectroscopy, in which the generation of small polarons due to the strong electron–phonon interaction was raised to explicate the anomalous negative terahertz photoconductivity [18]. Terahertz spectroscopy is sensitive to the free carrier but insensitive to the excited electronic states and the coherent phonons. In contrast, optical spectroscopy is a

standard tool for investigating the recovery process of carriers at various excited states as well as the generation and dynamical evolution of coherent phonon in solids [19,20]. What is more, so far as we have learned till now, the photoresponse in optical frequency and coherent phonon dynamics in $PtTe_2$ are obscured and urgently need to be unveiled. On the one hand, it is crucial to elucidate the excited-state dynamics for the study of many-body phenomena and light–matter interaction on ultrafast time scales. On the other hand, the exploration for coherent phonons allows significant insight into the microscopic essence of optically driven and controlled lattice or atomic motion.

Herein, the photoexcited carrier and coherent phonon dynamics in type-II DSM $PtTe_2$ films have been investigated systematically at room temperature with ultrafast pump-probe spectroscopy. The cooling of the thermal carriers plays a leading role in the incoherent relaxation processes. The temperature gradient is responsible for the generation of the CAP in the thicker sample. The COP is also observed in $PtTe_2$ films, which has been assigned to the A_{1g} optical phonon mode. The present study sheds light on the photocarrier and coherent phonon dynamics, which are of paramount importance to explore the applications of $PtTe_2$ in ultrafast optoelectronic and nanoscale devices.

2. CHARACTERIZATIONS AND EXPERIMENTAL SETUP

Homogeneous and continuous $PtTe_2$ films with thicknesses of 6.8 and 20 nm were synthesized on fused silica substrate via a novel eutectic solidification method [10]; the lateral size is 10 mm × 10 mm. More detailed characterizations about our measured films, including atomic force microscopy, X-ray diffraction, X-ray photoemission spectra, etc., have been shown in our previous work [18].

Ultrafast time-resolved degenerate optical pump-optical probe (OPOP) measurements in transmission configuration were performed with a home-built system. The optical pulses at a central wavelength of 780 nm (1.59 eV) are delivered from a Ti:sapphire regenerative amplifier (Spectra Physics, Spitfire) with single pulse energy of 2 mJ, pulse duration of 120 fs, and repetition rate of 1 kHz. The laser beam was split into the intense pump and weak probe beams, which were focused on the sample, overlapping with the pump spot estimated to be 0.67 mm in diameter, which is roughly twice as large as the probe beam. The fluence of probe light was fixed at about 114 $\mu J/cm^2$ [21,22]. To further explore the wavelength-dependent photocarrier and coherent phonon dynamics, transient absorption (TA) measurements were implemented, where the commercial TA spectrometer (HELIOS, Ultrafast System) is driven by a Ti:sapphire laser (Coherent, Astrella). The laser output optical pulses centered at 800 nm with a pulse duration of 35 fs and repetition rate of 1 kHz were divided into two beams: one was guided into an optical parametric amplifier to produce 780 nm excitation light; the other was focused on a sapphire slice to generate white light supercontinuum with a pulse duration of 150 fs, which serves as probe beam in the ultrafast system [23–25]. An optical filter was used to remove the redundant fundamental 800 nm beam and NIR parts of the supercontinuum beam. The pump fluence on the samples was fixed at around 1.0 mJ/cm^2, which was 10 times higher than that of the probe beam. The samples were placed on a holder and moved within a 1 mm × 1 mm plane perpendicular to the probe light propagation direction to avoid thermal accumulation. All the measurements were carried out at room temperature.

3. RESULTS AND DISCUSSION

The degenerate 780 nm OPOP measurement was first performed to investigate the excited carrier and coherent phonon dynamics of $PtTe_2$ films. The differential transmission response $\Delta T/T_0$ was recorded through varying pump-probe time delay, where T_0 is the linear optical transmission of probe light without photoexcitation, and the ΔT denotes photoinduced transmission change. In Fig. 1, we plot the transient transmission dynamics of 6.8 and 20 nm $PtTe_2$ films with various pump fluences. For 6.8 nm $PtTe_2$, as shown in Fig. 1(a), photoexcitation triggers an immediate rise in transmission, also known as photobleaching (PB), with response time limited by the laser pulse duration, followed by two distinct relaxation processes. The rapid recovery (τ_f) occurs within a subpicosecond time scale, followed by a slower relaxation (τ_s) lasting more than a hundred ps. For comparison, the 20 nm $PtTe_2$ film undergoes a rapid recovery, followed by a slight oscillation within the initial 40 ps; further, a slow relaxation is seen to dominate the subsequent signal. Figures 1(c) and 1(d) display the pump-fluence dependent peak value of $\Delta T/T_0$ and the linear fitting, which indicate the transient transmission response does not exhibit saturation in the range of pump fluence that we applied.

We now discuss the underlying physical origins that caused the ultrafast optical response. In general, the differential transmission signal $\Delta T/T_0$ is determined by electronic excitations (excited carriers) and/or lattice excitations (coherent phonons). In a semimetal like $PtTe_2$, the ultrashort optical pump pulses generally excite amounts of photocarriers into a nonequilibrium state characterized by valence band depletion and conduction band filling. Subsequently, the photocarrier thermalization occurs on tens of fs time scale via electron-electron (e-e) scattering, and establishes a hot-carrier distribution with a broadening energy range [26–28]. For the two $PtTe_2$ films, the instantaneous PB signals upon photoexcitation originate from the electrons' distribution in the conduction band due to the transition of electrons from the valence band into the conduction band by absorbing the pump photons, which block the corresponding interband transitions, i.e., Pauli-blocking or band filling effect [29,30]. Higher pump fluence means the more serious occupation of probing states, resulting in a stronger PB signal, which is coincident with our measurements, as shown in Figs. 1(c) and 1(d). Since the photocarrier thermalization is accomplished in an ultrashort time scale (within 100 fs), which is beyond our temporal resolution, it is a reasonable assignment that the photocarrier thermalization is completed in the ascending process of transient transmission.

To quantitatively evaluate the quasiparticle relaxation dynamics, a biexponential decay function convoluted with laser pulse width with the below form [24,31] was utilized to fit the transient profile:

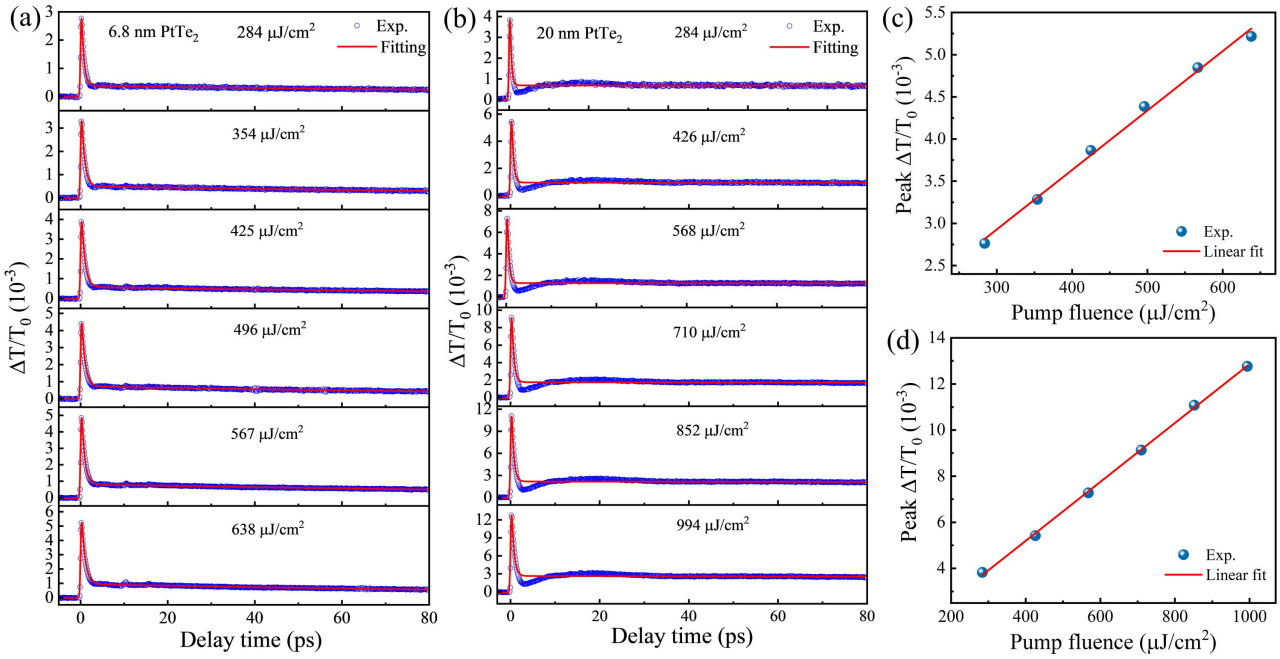

Fig. 1. Time-resolved transient transmission trace $\Delta T/T_0$ of (a) 6.8 nm and (b) 20 nm $PtTe_2$ films under various pump fluences with pumping and probing at 780 nm. Blue circles denote experimental data; red solid lines are the fitting curves with convoluted biexponential decay function. The peak $\Delta T/T_0$ versus pump fluence for (c) 6.8 nm and (d) 20 nm $PtTe_2$ films; red solid lines are the linear fitting.

$$\frac{\Delta T}{T_0}(t) = \sum_{i=1,2} A_i \cdot \exp\left(\frac{-t}{\tau_i} + \frac{\omega^2}{4\tau_i^2}\right) \cdot \left[1 - \mathrm{erf}\left(\frac{-t}{\omega} + \frac{\omega}{2\tau_i}\right)\right] + B, \quad (1)$$

where t is the pump-probe delay time, τ_i and A_i are the correlative relaxation constant and amplitude, respectively, and B is the time-independent offset. The erf represents the error function and ω is the cross-correlation width. For the 6.8 nm specimen, as shown in Fig. 1(a), one can see that the experimental data can be well reproduced with Eq. (1). By comparison, for the 20 nm $PtTe_2$ film, the transient transmission is seen to consist of two components; i.e., a coherent low-frequency oscillation is superimposed on the incoherent carrier relaxation profile. It is reasonable to ignore the low-frequency oscillation and employ a biexponential function to extract the photocarriers' lifetime. The fitting time constants τ_f are presented in Figs. 2(a) and 2(b). For the 6.8 nm film, the fast component has a lifetime τ_f of 0.51–0.81 ps with a weight of ~90%. While for 20 nm $PtTe_2$, the fast recovery shows a lifetime τ_f of 0.32–0.52 ps with a weight of ~90%. The fitted slow relaxation for both films shows an almost identical lifetime of longer than 100 ps with weight of less than 10%. It should be mentioned that the obtained slow lifetime is not accurate due to the limited scanning time window. Here, we ascribe the fast relaxation process of both samples to the cooling of the hot carriers that relax to conduction band edge via electron-optical phonon interaction, which is similar to what has been observed in other semimetal materials [32–35]. Higher pump fluence implies higher electronic temperature; hence, more elastic impact with lattice is needed to release their excess energy, resulting in a longer relaxation time, as shown in Figs. 2(a) and 2(b). One can note that τ_f of 20 nm film is shorter than that of 6.8 nm film, which is owing to the fact that the thicker sample has relatively larger electron–phonon coupling in $PtTe_2$ [18]; thus, the thermal carriers in 20 nm $PtTe_2$ have higher cooling efficiency. The slow component with insignificant weight for both films can be attributed to the interband recombination of electrons in the conduction band bottom and holes in the valence band top with the assist of phonon. Specifically, the type-II DSM $PtSe_2$, an analogue of $PtTe_2$, also shows hundreds of ps lifetimes in carrier recombination [24,29]. Therefore, we can reasonably assign the slow dynamics to electron-hole recombination.

We now focus on the oscillatory response observed in 20 nm $PtTe_2$. Figure 2(c) displays the low-frequency oscillation after subtracting the biexponential relaxation from the total dynamics trace at pump fluence of 994 $\mu J/cm^2$. The inset shows the frequency domain of the damped oscillation after fast Fourier transform (FFT) and gives the broader oscillation frequencies of 0–0.2 THz with the central frequency at 21.7 GHz. Further, the central frequencies obtained from FFT under other pump fluences are almost identical. Herein, we assign the low-frequency oscillation to CAP, i.e., the coherent lattice vibration with acoustic-mode gives rise to a modulation of the transmissivity of the probe beam.

As a matter of fact, upon ultrafast photoexcitation, the surface layers of material absorb the pump photon, bringing about a transient temperature rise via electron–phonon scattering within the illuminated area. Such sudden temperature elevation sets up localized transient stress, which induces a strain wave, i.e., coherent longitudinal acoustic phonon (CLAP), due to thermal expansion caused by the spatial temperature gradient

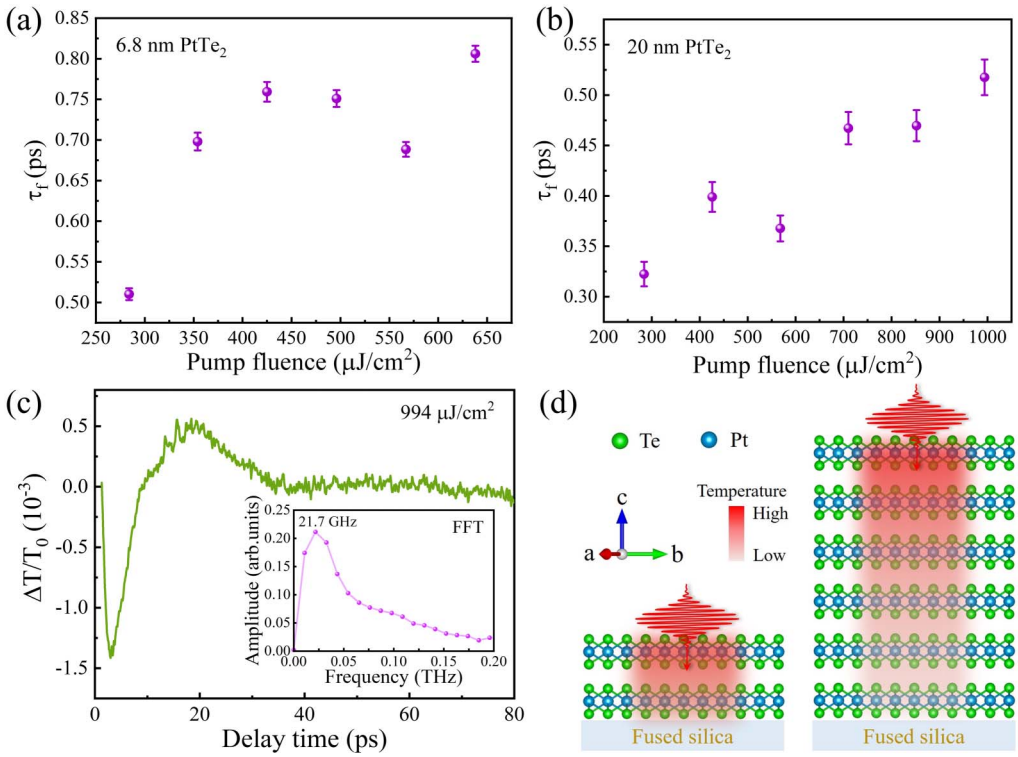

Fig. 2. Fitting fast lifetime τ_f of (a) 6.8 nm and (b) 20 nm $PtTe_2$ with a convoluted biexponential decay function with respect to pump fluence. (c) The extracted coherent acoustical phonon oscillatory signal by subtracting the fitted incoherent carrier dynamics from total transient trace under pump fluence of 994 $\mu J/cm^2$. Inset shows the frequency domain after FFT. (d) Schematic diagrams of CAP generation induced by temperature gradient. The left and right drawings respectively express the temperature response of 6.8 and 20 nm $PtTe_2$ films upon laser irradiation.

of material [36–39]. The CLAP propagates away from the surface of the material in the direction of the temperature gradient at sound speed, which modifies the local dielectric constant. When the delayed probe light is incident onto the material overlapped with a pump pulse, the transmissivity of probe light will be modified by the local modulated dielectric function thanks to the launch of CLAP. Therefore, the transmission change characterized by periodic oscillation can be sampled [22,40].

Figure 2(d) visualizes the different thermal responses to ultrafast laser irradiation in the thin and thick films, in which the gradient force is essential in driving the generation of CAP [38]. When the film is thin, as in our case of 6.8 nm, the photo-driven thermalization of the film is homogeneous in the propagation direction of pump pulse, as illustrated on the left drawing in Fig. 2(d). The absence of a temperature gradient signifies that the strain wave cannot be delivered, which is why we did not observe the CAP in 6.8 nm $PtTe_2$. In our 20 nm film, the photoexcitation from the front surface can induce a temperature gradient along the light propagation direction; as a result, the CAP is launched, as illustrated on the right drawing in Fig. 2(d). It should be mentioned that the pump-pulse-induced coherent acoustic vibration of the lattice in 20 nm $PtTe_2$ is not monochromatic but broadband. The sound velocity, v, can be determined with $v = 4df$ [36,40], with the d and f denoting the film thickness and CAP frequency. Considering $f = 21.7$ GHz obtained from $d = 20$ nm film the sound velocity in $PtTe_2$ film is obtained to be $v = 1.736$ km/s. By using the density of $\rho = 9.8 \times 10^3$ kg/m^3 for bulk $PtTe_2$ [41], Young's modulus (Y) of the film can be evaluated by

$$Y = \rho v^2 \tag{2}$$

from which $Y = 29.5$ GPa is obtained in the 20 nm $PtTe_2$ film according to our CAP measurement. It is close to Young's modulus of $PtSe_2$ with 28 GPa [39] but less than that in most TMDs with a value around 50 GPa [42], indicating $PtTe_2$ is a softer layered matter. To our knowledge, this is the first time that the sound velocity and Young's modulus in $PtTe_2$ are determined experimentally.

To gain more insight into probing the wavelength-dependent carrier and coherent phonon dynamics of 6.8 and 20 nm $PtTe_2$, TA measurements were carried out with pumping at 780 nm and probing at 450–760 nm. Figure 3 shows the TA pseudocolor plots and TA spectra, in which ΔA denotes the pump-induced absorption change of the probe pulse. It can be seen that the optical response of all probe light shows a negative TA signal, i.e., PB. The CAP is persistently present at all probe wavelengths for 20 nm $PtTe_2$, which is manifested as the appearance of a bottleneck-like color plot around the time window of 1–10 ps as an arrow indicated in Fig. 3(c). In contrast, this phenomenon is absent in the 6.8 nm sample. Unexpectedly, pronounced damping harmonic oscillations were observed at the early probe delays; more detailed color mappings of TA in the first 5 ps are shown in Fig. 5 of Appendix A.

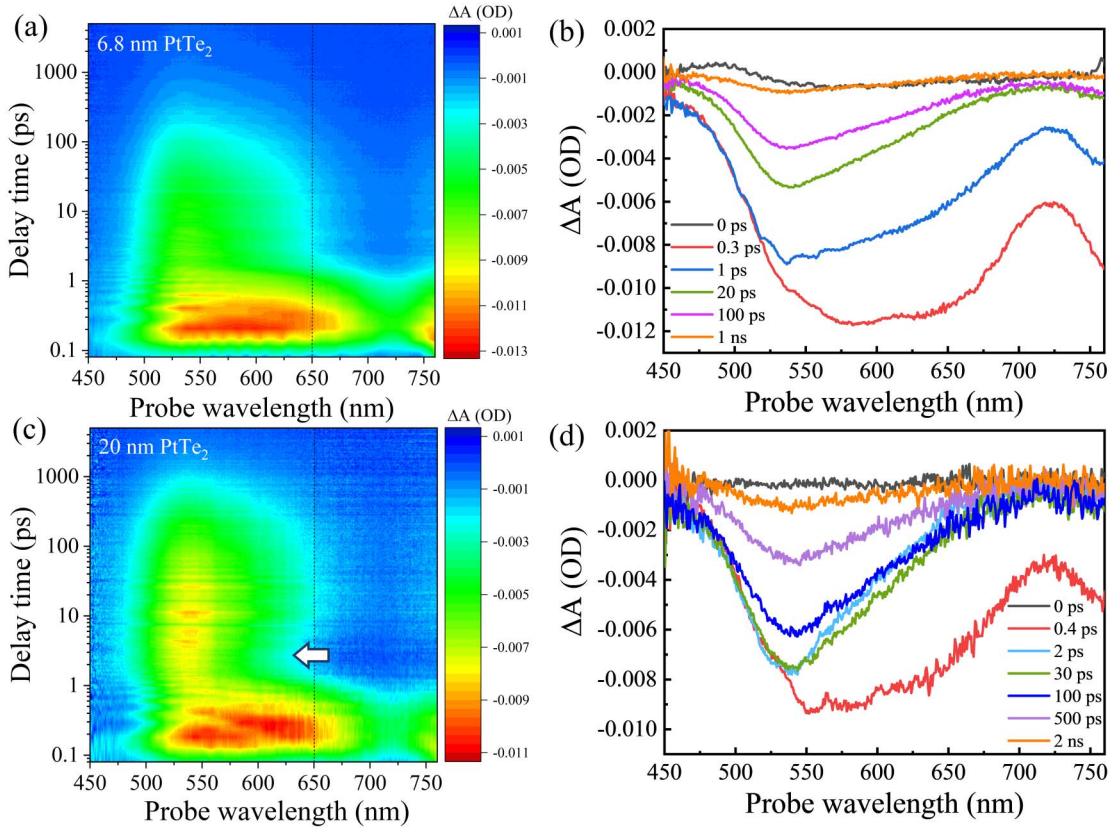

Fig. 3. Time- and spectrum-resolved ultrafast TA mapping of (a) 6.8 nm $PtTe_2$ and (c) 20 nm $PtTe_2$ photoexcited by 780 nm fs pump pulse with constant 1 mJ/cm^2 pump fluence. The unit OD denotes optical density. The TA spectrum of (b) 6.8 nm and (d) 20 nm $PtTe_2$ at several selected time delays.

We first discuss the relaxation of the electronic system under different probe energy. The general profile of photocarriers' relaxation of 6.8 and 20 nm films is mostly the same. One prominent feature is that the dynamics of the red and blue sides around 650 nm [as the marks of black dash lines in Figs. 3(a) and 3(c)] are distinct. The relaxation of red side, i.e., 650–760 nm, consists of two components: a subpicosecond fast relaxation followed by a slow process with a lifetime of more than 100 ps, which is similar to the experimental results measured with degenerate 780 nm OPOP. By comparison, the relaxation of the blue side of 650 nm shows an extra slow component except for the fast and slow processes. This slow process has a time constant of a few nanoseconds, which reflects the long-lived electronic states at the higher-lying energy band in $PtTe_2$.

The coherent collective excitations with probe wavelength dependence in $PtTe_2$ are displayed in Figs. 4(a) and 4(c) for 20 and 6.8 nm films, respectively. Apparently, all curves can be treated as the superposition of the nonoscillatory background derived from electronic contribution and high-frequency coherent phonon oscillations; in addition, CAP also contributes to the TA kinetics in the 20 nm $PtTe_2$. Following the aforementioned approach of obtaining CAP oscillation, we have unwrapped the high-frequency damped oscillation component. Figures 4(b) and 4(d), respectively, exemplify the pure time-domain oscillation (green) of 20 and 6.8 nm film at a typical probe wavelength of 525 nm. For the sake of simplification, measuring results of 6.8 nm $PtTe_2$ are dissected thoroughly; more detailed oscillatory signals of 6.8 nm $PtTe_2$ under different probe wavelengths are shown in Fig. 6 of Appendix A. The corresponding frequency domain of the oscillation after FFT is also plotted in the insets of Figs. 4(b) and 4(d), yielding a sharp high-frequency mode of 4.7 THz for 20 nm film and 4.65 THz for 6.8 nm film. Furthermore, a one-component damped oscillation function with the below formula was used to fit the oscillations for further analysis:

$$\Delta A(t)_{\mathrm{OSC}} = B \cdot \exp\left(-\frac{t-t_0}{\tau}\right) \cdot \cos(2\pi f t + \phi) + C, \quad \textbf{(3)}$$

where B, τ, f, and ϕ are the oscillatory signal amplitude, damping time, frequency, and initial phase, respectively, which describe the collective excitation dynamics. As displayed in Figs. 4(b) and 4(d), one can see that the experimental data can be reproduced well, and the fitting frequency is 4.70 THz for 20 nm $PtTe_2$ and 4.66 THz for 6.8 nm, which are consistent with FFT results. The dephasing time obtained by fitting is around 2.8 ps and almost independent of the probe wavelength, as shown in Fig. 7 of Appendix A. Figure 4(e) shows the Raman spectrum of 20 nm $PtTe_2$, where two phonon modes, i.e., E_g (112 cm^{-1}) and A_{1g} (156 cm^{-1}, ~4.68 THz), can be observed clearly. The E_g and A_{1g} modes originate from the vibration of Te atoms along the in-plane and

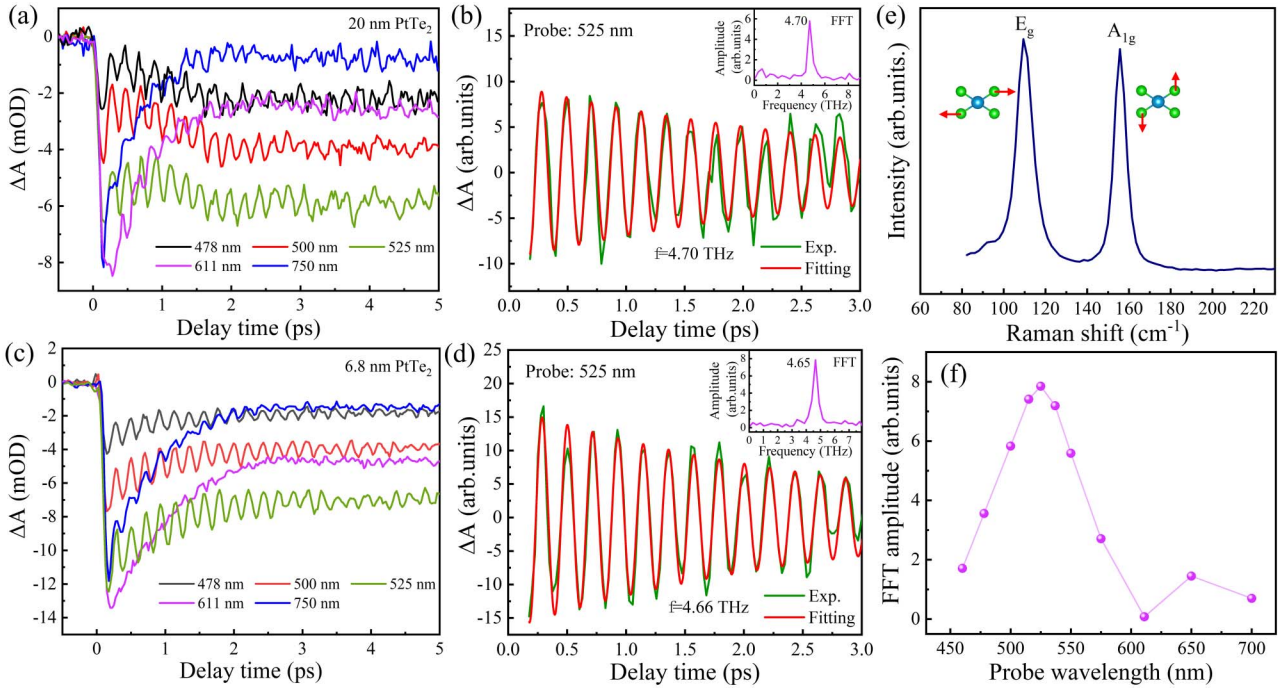

Fig. 4. Probe wavelength-dependent COP dynamics of $PtTe_2$ film. TA kinetics in the first 5 ps of (a) 20 nm and (c) 6.8 nm $PtTe_2$ at selective representative probe wavelengths. Extracted typical optical phonon oscillation at 525 nm and the fitting curve of (b) 20 nm and (d) 6.8 nm $PtTe_2$, in which the inset denotes the FFT amplitude spectrum. (e) The 532 nm Raman spectrum of 20 nm $PtTe_2$; the red arrows indicate the motion direction of the Te atom. (f) The FFT amplitude of residual oscillations of 6.8 nm $PtTe_2$ as a function of the probe wavelength.

out-of-plane, respectively. Extracted frequency of periodic oscillations is identical to that of A_{1g} phonon, which suggests the coherent damping oscillations in $PtTe_2$ under photoexcitation emanated from the A_{1g} optical phonon, that is, the pump-induced coherent vibration of atoms in each unit cell with A_{1g} mode modulates periodically the index of absorption.

In general, two mechanisms have been proposed to explicate the generation of COP excited by ultrafast optical pulse: impulsive stimulated Raman scattering (ISRS) and displacive excitation of coherent phonon (DECP) [43–45]. In the ISRS mechanism, an ultrashort laser pulse (pulse duration must be shorter compared with the oscillatory period of lattice), which has a distribution of frequency containing ω_1 and ω_2, coupled to phonon mode with the energy of $\hbar\omega_0$ ($\omega_0 = \omega_1 - \omega_2$), exerting an "impulsive" driving force for coherent vibrations of lattice [46–50]. In the DECP model, the excitation of COP is due to a displacement of the ion equilibrium coordinates by electronic excitation [51]. The pump pulse creates excited carriers, leading to electronic redistribution and thus initiating the ion cores to vibration coherently around the new equilibrium positions, which is the refined picture of the DECP model [38,52,53]. Noticeably, the Raman scattering mechanism allows all coherent phonon excitation with Raman-active modes, while the DECP mechanism only favors the excitation of totally symmetric modes (e.g., A_{1g}) [45,51,52]. Consequently, the DECP is responsible for the excitation of the A_{1g} mode only in our observation. Another conspicuous feature is that the strength of the oscillation is seen to vary significantly with probe wavelength, as shown in Figs. 4(a), 4(c), and Fig. 6 of Appendix A, respectively. Figure 4(f) plots the FFT amplitude of the residual oscillations of 6.8 nm $PtTe_2$ with respect to the probe wavelength. The amplitude of oscillatory signal depends on the probe wavelength, with a maximum around 525 nm; further, no appreciable oscillations above 600 nm were detected in the resolution of our apparatus. We assign the probe wavelength-dependent oscillatory response to the different band modulation induced by the A_{1g} phonon displacement.

Essentially, ultrafast photoexcitation leads to a displacement of the Te atoms along the outward direction, in turn causing a change in the energy band structure, accompanied by a modulation of optical constants. The coherent vibration of the atoms induced by the A_{1g} mode around the displaced equilibrium positions leads to the dynamical change of energy bands and the period modulation of the optical absorption, which manifests as the oscillations in the TA kinetics [45,54,55]. The probe wavelength-dependent COP strength is due to the fact that the atomic displacement induced by DECP has different influence on the energy bands at different locations. Thus, it can be deduced that the energy band associated with the electronic transition of 2.4 eV (525 nm), somewhere in the Brillouin zone, is most significantly influenced, while atomic displacement shows negligible effect on the electronic transition below 2.1 eV (600 nm). In-depth analysis of the changed band structures needs more elaborate *ab initio* calculations [54], which are beyond the scope of this work. In a word, the study herein offers a channel to monitor the dispersion of the variation in optical parameters in a photoexcited nonequilibrium state through tracking the different oscillatory strengths of TA kinetics induced by COP. Moreover, our differential

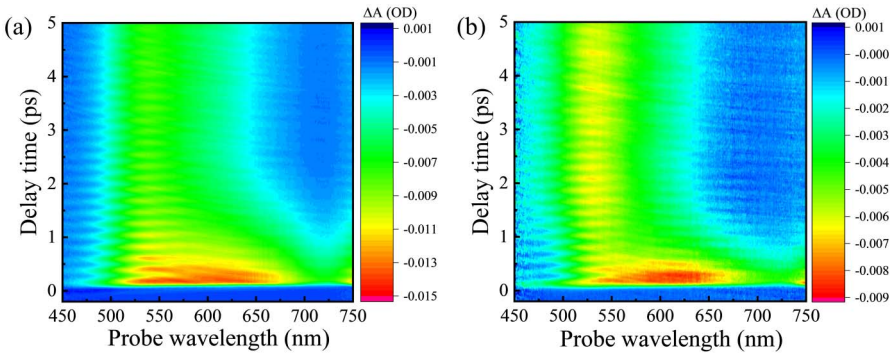

Fig. 5. The TA plotting of (a) 6.8 nm and (b) 20 nm $PtTe_2$ film in the initial 5 ps of time delay.

transmission study has also provided a wealth of information on COP modes in the time domain.

4. CONCLUSION

In summary, the ultrafast OPOP measurements were conducted to uncover the photocarriers' relaxation dynamics and the generation mechanisms of coherent phonon in type-II DSM $PtTe_2$ films. The inherent electronic recovery process is predominantly dominated by the cooling of thermal carriers. CAP and COP arise from the inhomogeneous temperature distribution in film and DECP, respectively. Our present study enriches the insight into $PtTe_2$ and will be helpful in predicting the change of electronic bands upon photoexcitation, which paves the way in designing and developing $PtTe_2$-based ultrafast optoelectronics.

APPENDIX A: THE OBSERVATION OF COP IN TA MEASUREMENTS

To more clearly show the damping oscillations induced by A_{1g} COP in TA mappings, the TA plots of $PtTe_2$ films in the first 5 ps of time delay are shown in Fig. 5. Figure 6 displays the extracted high-frequency oscillatory signals for 6.8 nm $PtTe_2$ at several selectively probe wavelengths, from which one can see

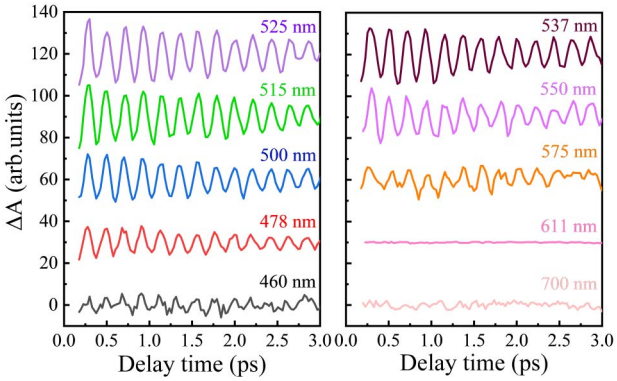

Fig. 6. Residual periodical oscillatory signals of 6.8 nm $PtTe_2$ film with respect to the probe wavelength in the time domain. The individual signal is obtained by subtracting the incoherent carrier dynamics from the total transient trace.

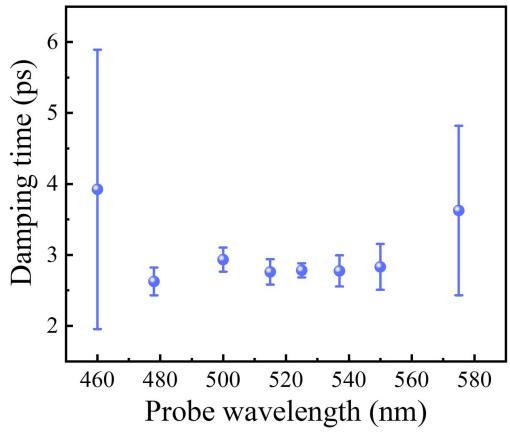

Fig. 7. Damping time of coherent optical phonon of 6.8 nm $PtTe_2$ film with respect to probe wavelength.

that the amplitude of the oscillatory signal exhibits a strong probe wavelength dependence. Probe wavelength-dependent damping time of A_{1g} COP is shown in Fig. 7, which is obtained by fitting the pure oscillatory signals with Eq. (3) in the main text. It can be seen that the damping time is mostly independent of probe wavelength, with an average lifetime of ~2.8 ps. The large error bars at 460 nm and 575 nm are due to the very small oscillatory amplitude at these two probe wavelengths.

Funding. National Natural Science Foundation of China (61735010, 92150101, 11774233, 62122036, 61974176).

Disclosures. The authors declare no conflicts of interest related to this paper.

REFERENCES

1. Z. K. Liu, B. Zhou, Y. Zhang, Z. J. Wang, H. M. Weng, D. Prabhakaran, M. Z. Mo, Z. X. Shen, Z. Fang, X. Dai, Z. Hussain, and Y. L. Chen, "Discovery of a three-dimensional topological Dirac semimetal, Na_3Bi," Science **343**, 864–867 (2014).
2. S.-Y. Xu, C. Liu, S. K. Kushwaha, R. Sankar, J. W. Krizan, I. Belopolski, M. Neupane, G. Bian, N. Alidoust, T.-R. Chang, H.-T. Jeng, C.-Y. Huang, W.-F. Tsai, H. Lin, P. P. Shibayev, F.-C. Chou, R. J. Cava, and M. Z. Hasan, "Observation of Fermi arc surface states in a topological metal," Science **347**, 294–298 (2015).

3. Z. K. Liu, J. Jiang, B. Zhou, Z. J. Wang, Y. Zhang, H. M. Weng, D. Prabhakaran, S. K. Mo, H. Peng, P. Dudin, T. Kim, M. Hoesch, Z. Fang, X. Dai, Z. X. Shen, D. L. Feng, Z. Hussain, and Y. L. Chen, "A stable three-dimensional topological Dirac semimetal Cd_3As_2," Nat. Mater. **13**, 677–681 (2014).
4. S. Borisenko, Q. Gibson, D. Evtushinsky, V. Zabolotnyy, B. Buchner, and R. J. Cava, "Experimental realization of a three-dimensional Dirac semimetal," Phys. Rev. Lett. **113**, 027603 (2014).
5. H.-J. Noh, J. Jeong, E.-J. Cho, K. Kim, B. I. Min, and B.-G. Park, "Experimental realization of type-II Dirac fermions in a $PdTe_2$ superconductor," Phys. Rev. Lett. **119**, 016401 (2017).
6. A. A. Soluyanov, D. Gresch, Z. Wang, Q. Wu, M. Troyer, X. Dai, and B. A. Bernevig, "Type-II Weyl semimetals," Nature **527**, 495–498 (2015).
7. M. Yan, H. Huang, K. Zhang, E. Wang, W. Yao, K. Deng, G. Wan, H. Zhang, M. Arita, H. Yang, Z. Sun, H. Yao, Y. Wu, S. Fan, W. Duan, and S. Zhou, "Lorentz-violating type-II Dirac fermions in transition metal dichalcogenide $PtTe_2$," Nat. Commun. **8**, 257 (2017).
8. A. Politano, G. Chiarello, B. Ghosh, K. Sadhukhan, C.-N. Kuo, C. S. Lue, V. Pellegrini, and A. Agarwal, "3D Dirac plasmons in the type-II Dirac semimetal $PtTe_2$," Phys. Rev. Lett. **121**, 086804 (2018).
9. L. Fu, D. Hu, R. G. Mendes, M. H. Rummeli, Q. Dai, B. Wu, L. Fu, and Y. Liu, "Highly organized epitaxy of Dirac semimetallic $PtTe_2$ crystals with extrahigh conductivity and visible surface plasmons at edges," ACS Nano **12**, 9405–9411 (2018).
10. S. Hao, J. Zeng, T. Xu, X. Cong, C. Wang, C. Wu, Y. Wang, X. Liu, T. Cao, G. Su, L. Jia, Z. Wu, Q. Lin, L. Zhang, S. Yan, M. Guo, Z. Wang, P. Tan, L. Sun, Z. Ni, S.-J. Liang, X. Cui, and F. Miao, "Low-temperature eutectic synthesis of $PtTe_2$ with weak antilocalization and controlled layer thinning," Adv. Funct. Mater. **28**, 1803746 (2018).
11. M. K. Lin, R. A. B. Villaos, J. A. Hlevyack, P. Chen, R. Y. Liu, C. H. Hsu, J. Avila, S. K. Mo, F. C. Chuang, and T. C. Chiang, "Dimensionality-mediated semimetal-semiconductor transition in ultrathin $PtTe_2$ films," Phys. Rev. Lett. **124**, 036402 (2020).
12. K. Deng, M. Yan, C.-P. Yu, J. Li, X. Zhou, K. Zhang, Y. Zhao, K. Miyamoto, T. Okuda, W. Duan, Y. Wu, X. Zhong, and S. Zhou, "Crossover from 2D metal to 3D Dirac semimetal in metallic $PtTe_2$ films with local Rashba effect," Sci. Bull. **64**, 1044–1048 (2019).
13. F. Fei, X. Bo, P. Wang, J. Ying, J. Li, K. Chen, Q. Dai, B. Chen, Z. Sun, M. Zhang, F. Qu, Y. Zhang, Q. Wang, X. Wang, L. Cao, H. Bu, F. Song, X. Wan, and B. Wang, "Band structure perfection and superconductivity in type-II Dirac semimetal $Ir_{1-x}Pt_xTe_2$," Adv. Mater. **30**, 1801556 (2018).
14. J. Jiang, S. Lee, F. Fei, F. Song, E. Vescovo, K. Kaznatcheev, F. J. Walker, and C. H. Ahn, "A comprehensive ARPES study on the type-II Dirac semimetal candidate $Ir_{1-x}Pt_xTe_2$," APL Mater. **8**, 061106 (2020).
15. X. W. Tong, Y. N. Lin, R. Huang, Z. X. Zhang, C. Fu, D. Wu, L. B. Luo, Z. J. Li, F. X. Liang, and W. Zhang, "Direct tellurization of Pt to synthesize 2D $PtTe_2$ for high-performance broadband photodetectors and NIR image sensors," ACS Appl. Mater. Interfaces **12**, 53921–53931 (2020).
16. M. S. Shawkat, S. B. Hafiz, M. M. Islam, S. A. Mofid, M. M. Al Mahfuz, A. Biswas, H. S. Chung, E. Okogbue, T. J. Ko, D. Chanda, T. Roy, D. K. Ko, and Y. Jung, "Scalable van der Waals two-dimensional $PtTe_2$ layers integrated onto silicon for efficient near-to-mid infrared photodetection," ACS Appl. Mater. Interfaces **13**, 15542–15550 (2021).
17. H. Xu, C. Guo, J. Zhang, W. Guo, C. N. Kuo, C. S. Lue, W. Hu, L. Wang, G. Chen, A. Politano, X. Chen, and W. Lu, "$PtTe_2$-based type-II Dirac semimetal and its van der Waals heterostructure for sensitive room temperature terahertz photodetection," Small **15**, 1903362 (2019).
18. P. Suo, H. Zhang, S. Yan, W. Zhang, J. Fu, X. Lin, S. Hao, Z. Jin, Y. Zhang, C. Zhang, F. Miao, S.-J. Liang, and G. Ma, "Observation of negative terahertz photoconductivity in large area type-II Dirac semimetal $PtTe_2$," Phys. Rev. Lett. **126**, 227402 (2021).
19. N. Kumar, B. A. Ruzicka, N. P. Butch, P. Syers, K. Kirshenbaum, J. Paglione, and H. Zhao, "Spatially resolved femtosecond pump-probe study of topological insulator Bi_2Se_3," Phys. Rev. B **83**, 235306 (2011).
20. A. Othonos, "Probing ultrafast carrier and phonon dynamics in semiconductors," J. Appl. Phys. **83**, 1789–1830 (1998).
21. J. Fu, M. Jiang, P. Suo, W. Zhang, X. Lin, X. Yan, S. Zhang, and G. Ma, "Optically controlled ultrafast terahertz switching in wafer scale $PtSe_2$ thin films," Appl. Opt. **60**, 5037–5043 (2021).
22. D. Li, J. Fu, P. Suo, W. Zhang, B. Lu, X. Lin, X. Yan, B. Li, G. Ma, and J. Yao, "Layer dependent interlayer coherent phonon dynamics in $PdSe_2$ films," Appl. Phys. Lett. **118**, 191105 (2021).
23. J. Wei, Y. Wu, R. Pu, L. Shi, J. Jiang, J. Du, Z. Guo, Y. Huang, and W. Liu, "Tracking ultrafast structural dynamics in a dual-emission anti-kasha-active fluorophore using femtosecond stimulated Raman spectroscopy," J. Phys. Chem. Lett. **12**, 4466–4473 (2021).
24. J. Fu, W. Xu, X. Chen, S. Zhang, W. Zhang, P. Suo, X. Lin, J. Wang, Z. Jin, W. Liu, and G. Ma, "Thickness-dependent ultrafast photocarrier dynamics in selenizing platinum thin films," J. Phys. Chem. C **124**, 10719–10726 (2020).
25. T. C. Sum, N. Mathews, G. Xing, S. S. Lim, W. K. Chong, D. Giovanni, and H. A. Dewi, "Spectral features and charge dynamics of lead halide perovskites: origins and interpretations," Acc. Chem. Res. **49**, 294–302 (2016).
26. M. Breusing, C. Ropers, and T. Elsaesser, "Ultrafast carrier dynamics in graphite," Phys. Rev. Lett. **102**, 086809 (2009).
27. C. Zhu, X. Yuan, F. Xiu, C. Zhang, Y. Xu, R. Zhang, Y. Shi, and F. Wang, "Broadband hot carrier dynamics in three-dimensional Dirac semimetal Cd_3As_2," Appl. Phys. Lett. **111**, 091101 (2017).
28. P. A. George, J. Strait, J. Dawlaty, S. Shivaraman, M. Chandrashekhar, F. Rana, and M. G. Spencer, "Ultrafast optical-pump terahertz-probe spectroscopy of the carrier relaxation and recombination dynamics in epitaxial graphene," Nano Lett. **8**, 4248–4251 (2008).
29. G. Wang, K. Wang, N. McEvoy, Z. Bai, C. P. Cullen, C. N. Murphy, J. B. McManus, J. J. Magan, C. M. Smith, G. S. Duesberg, I. Kaminer, J. Wang, and W. J. Blau, "Ultrafast carrier dynamics and bandgap renormalization in layered $PtSe_2$," Small **15**, 1902728 (2019).
30. H. Haug and S. W. Koch, *Quantum Theory of the Optical and Electronic Properties of Semiconductors* (World Scientific, 2009).
31. R. P. Prasankumar and A. J. Taylor, *Optical Techniques for Solid-State Materials Characterization* (CRC Press, 2016).
32. W. Lu, S. Ge, X. Liu, H. Lu, C. Li, J. Lai, C. Zhao, Z. Liao, S. Jia, and D. Sun, "Ultrafast relaxation dynamics of photoexcited Dirac fermions in the three-dimensional Dirac semimetal Cd_3As_2," Phys. Rev. B **95**, 024303 (2017).
33. Y. M. Dai, J. Bowlan, H. Li, H. Miao, S. F. Wu, W. D. Kong, Y. G. Shi, S. A. Trugman, J. X. Zhu, H. Ding, A. J. Taylor, D. A. Yarotski, and R. P. Prasankumar, "Ultrafast carrier dynamics in the large-magnetoresistance material WTe_2," Phys. Rev. B **92**, 161104 (2015).
34. S.-X. Zhu, C. Zhang, Q.-Y. Wu, X.-F. Tang, H. Liu, Z.-T. Liu, Y. Luo, J.-J. Song, F.-Y. Wu, Y.-Z. Zhao, S.-Y. Liu, T. Le, X. Lu, H. Ma, K.-H. Liu, Y.-H. Yuan, H. Huang, J. He, H. Y. Liu, Y.-X. Duan, and J.-Q. Meng, "Temperature evolution of quasiparticle dispersion and dynamics in semimetallic 1T-$TiTe_2$ via high-resolution angle-resolved photoemission spectroscopy and ultrafast optical pump-probe spectroscopy," Phys. Rev. B **103**, 115108 (2021).
35. Y. M. Sheu, Y. J. Chien, C. Uher, S. Fahy, and D. A. Reis, "Free-carrier relaxation and lattice heating in photoexcited bismuth," Phys. Rev. B **87**, 075429 (2013).
36. C. Thomsen, J. Strait, Z. Vardeny, H. J. Maris, J. Tauc, and J. J. Hauser, "Coherent phonon generation and detection by picosecond light pulses," Phys. Rev. Lett. **53**, 989–992 (1984).
37. C. Thomsen, H. T. Grahn, H. J. Maris, and J. Tauc, "Surface generation and detection of phonons by picosecond light pulses," Phys. Rev. B **34**, 4129–4138 (1986).
38. Y. Wang, L. Guo, X. Xu, J. Pierce, and R. Venkatasubramanian, "Origin of coherent phonons in Bi_2Te_3 excited by ultrafast laser pulses," Phys. Rev. B **88**, 064307 (2013).
39. X. Chen, S. Zhang, L. Wang, Y.-F. Huang, H. Liu, J. Huang, N. Dong, W. Liu, I. M. Kislyakov, J. M. Nunzi, L. Zhang, and J. Wang, "Direct observation of interlayer coherent acoustic phonon dynamics in bilayer and few-layer $PtSe_2$," Photon. Res. **7**, 1416–1424 (2019).

40. S. Ge, X. Liu, X. Qiao, Q. Wang, Z. Xu, J. Qiu, P. H. Tan, J. Zhao, and D. Sun, "Coherent longitudinal acoustic phonon approaching THz frequency in multilayer molybdenum disulphide," Sci. Rep. **4**, 5722 (2014).
41. S. Soled, A. Wold, and O. Gorochov, "Crystal growth and characterization of platinum ditelluride," Mat. Res. Bull. **10**, 831–836 (1975).
42. F. Vialla and N. D. Fatti, "Time-domain investigations of coherent phonons in van der Waals thin films," Nanomaterials **10**, 2543 (2020).
43. K. J. Yee, Y. S. Lim, T. Dekorsy, and D. S. Kim, "Mechanisms for the generation of coherent longitudinal-optical phonons in GaAs/AlGaAs multiple quantum wells," Phys. Rev. Lett. **86**, 1630–1633 (2001).
44. A. R. Attar, H. T. Chang, A. Britz, X. Zhang, M. F. Lin, A. Krishnamoorthy, T. Linker, D. Fritz, D. M. Neumark, R. K. Kalia, A. Nakano, P. Ajayan, P. Vashishta, U. Bergmann, and S. R. Leone, "Simultaneous observation of carrier-specific redistribution and coherent lattice dynamics in 2H-$MoTe_2$ with femtosecond core-level spectroscopy," ACS Nano **14**, 15829–15840 (2020).
45. J. Fu, M. Li, A. Solanki, Q. Xu, Y. Lekina, S. Ramesh, Z. X. Shen, and T. C. Sum, "Electronic states modulation by coherent optical phonons in 2D halide perovskites," Adv. Mater. **33**, 2006233 (2021).
46. Y.-X. Yan, E. B. Gamble, and K. Nelson, "Impulsive stimulated scattering: general importance in femtosecond laser pulse interactions with matter, and spectroscopic applications," J. Chem. Phys. **83**, 5391–5399 (1985).
47. S. D. Silvestri, J. G. Fujimoto, E. P. Ippen, E. B. Bamble, Jr., L. R. Williams, and K. A. Nelson, "Femtosecond time-resolved measurements of optic phonon dephasing by impulsive stimulated Raman scattering in α-perylene crystal from 20 to 300 K," Chem. Phys. Lett. **116**, 146–152 (1985).
48. A. M. Weiner, D. E. Leaird, G. P. Wiederrecht, and K. Nelson, "Femtosecond pulse sequences used for optical manipulation of molecular motion," Science **247**, 1317–1319 (1990).
49. G. C. Cho, W. Kutt, and H. Kurz, "Subpicosecond time-resolved coherent-phonon oscillations in GaAs," Phys. Rev. Lett. **65**, 764–766 (1990).
50. L. Dhar, J. A. Rogers, and K. A. Nelson, "Time-resolved vibrational spectroscopy in the impulsive limit," Chem. Rev. **94**, 157–193 (1994).
51. T. K. Cheng, J. Vidal, H. J. Zeiger, G. Dresselhaus, M. S. Dresselhaus, and E. P. Ippen, "Mechanism for displacive excitation of coherent phonons in Sb, Bi, Te, and Ti_2O_3," Appl. Phys. Lett. **59**, 1923–1925 (1991).
52. H. J. Zeiger, J. Vidal, T. K. Cheng, E. P. Ippen, G. Dresselhaus, and M. S. Dresselhaus, "Theory for displacive excitation of coherent phonons," Phys. Rev. B **45**, 768–778 (1992).
53. G. A. Garrett, T. F. Albrecht, J. F. Whitaker, and R. Merlin, "Coherent THz phonons driven by light pulses and the Sb problem: what is the mechanism?" Phys. Rev. Lett. **77**, 3661–3664 (1996).
54. C. Trovatello, H. P. C. Miranda, A. Molina-Sanchez, R. Borrego-Varillas, C. Manzoni, L. Moretti, L. Ganzer, M. Maiuri, J. Wang, D. Dumcenco, A. Kis, L. Wirtz, A. Marini, G. Soavi, A. C. Ferrari, G. Cerullo, D. Sangalli, and S. D. Conte, "Strongly coupled coherent phonons in single-layer MoS_2," ACS Nano **14**, 5700–5710 (2020).
55. T. Y. Jeong, B. M. Jin, S. H. Rhim, L. Debbichi, J. Park, Y. D. Jang, H. R. Lee, D. H. Chae, D. Lee, Y. H. Kim, S. Jung, and K. J. Yee, "Coherent lattice vibrations in mono- and few-layer WSe_2," ACS Nano **10**, 5560–5566 (2016).